Broad Emission Line Analysis and Black Hole Mass Estimation for the Type-1 Quasar SDSS J000111.19-002011.5

Serat Mahmud Saad[1] and Radh Chowdhury[2]

[1]*Department of Astronomy, Ohio State University, Ohio, USA*
[2]*Student, Notre Dame College, Dhaka, Bangladesh*

ABSTRACT

We present a comprehensive spectroscopic analysis of the Type-1 quasar SDSS J000111.19-002011.5 (Hereafter SDSS J000111) at redshift $z = 0.5178$, selected from the Sloan Digital Sky Survey (SDSS) Baryon Oscillation Spectroscopic Survey (BOSS). We perform multi-component spectral decomposition of both the Hβ–[O III] region (rest-frame 4700–5100 Å) and the Hα–[N II]–[S II] region (rest-frame 6400–6800 Å), employing power-law continuum modeling, Fe II and stellar template subtraction, and multi-Gaussian emission line fitting. From the broad Balmer components, we measure full widths at half maximum of $\mathrm{FWHM_{H\beta}} = 4277$ km s^{-1} and $\mathrm{FWHM_{H\alpha}} = 4707$ km s^{-1}. Using established single-epoch virial calibrations, we derive black hole mass estimates ranging from $M_{\mathrm{BH}} \sim 10^{6.4}$ to $10^{9.0}$ $M_\odot$ depending on the calibration employed. We discuss the systematic uncertainties inherent in single-epoch mass estimates and the implications of the observed line properties for the structure of the broad-line region.

Keywords: galaxies: active — galaxies: nuclei — quasars: emission lines — quasars: supermassive black holes — techniques: spectroscopic

1. INTRODUCTION

1.1. *Active Galactic Nuclei and Supermassive Black Holes*

Active galactic nuclei (AGN) are among the most luminous persistent sources in the universe, powered by accretion onto supermassive black holes (SMBHs) with masses ranging from $\sim 10^6$ to 10^{10} $M_\odot$ (Kormendy & Ho 2013). The study of AGN provides unique insights into black hole demographics, galaxy evolution, and the physics of accretion under extreme conditions. Since the discovery of quasars in the early 1960s (Schmidt 1963), AGN research has revealed a diverse phenomenology unified by the central engine paradigm: a SMBH surrounded by an accretion disk, broad-line region (BLR), dusty torus, and narrow-line region (NLR) at progressively larger scales (Antonucci 1993; Urry & Padovani 1995; Netzer 2015).

The classification of AGN into Type-1 and Type-2 categories reflects viewing angle effects relative to the obscuring torus (Antonucci & Miller 1985). Type-1 AGN, viewed at relatively face-on orientations, display both broad permitted emission lines (FWHM $\gtrsim$ 1000 km s^{-1}) originating in the BLR and narrow forbidden lines (FWHM $\lesssim$ 500 km s^{-1}) from the more extended NLR. The broad lines serve as direct probes of the gravitational potential of the central black hole, enabling mass measurements through the virial theorem (Peterson 1993; Peterson et al. 2004).

1.2. *Broad-Line Region Physics and Emission Line Diagnostics*

The broad-line region consists of dense ($n_e \sim 10^9$–10^{11} cm^{-3}) gas clouds located at distances of ~ 0.01–1 pc from the central ionizing source (Peterson 1993; Bentz et al. 2013). The large velocity widths observed in broad permitted lines—typically 1000–20000 km s^{-1}—arise from the Keplerian or virialized motion of this gas under the gravitational influence of the SMBH. The Balmer series lines, particularly Hα λ6563 and Hβ λ4861, are the most commonly used broad-line diagnostics due to their strength and accessibility in the optical wavelength range (Greene & Ho 2005).

The Hβ emission line, together with the adjacent 5100 Å continuum luminosity, forms the foundation of the reverberation mapping technique and its single-epoch mass estimation extensions (Kaspi et al. 2000, 2005; Bentz et al. 2013). The Hα line offers complementary advantages: it is intrinsically stronger than Hβ by a factor of ~ 3 (Case B recombination), suffers less dust

extinction, and remains accessible at higher redshifts before shifting into the near-infrared (Greene & Ho 2005). Using both Balmer lines provides a valuable consistency check and reduces systematic uncertainties in mass estimates.

The narrow-line region, extending from tens of parsecs to kiloparsec scales, produces forbidden emission lines that serve as powerful diagnostics of the ionization mechanism.

1.3. *Black Hole Mass Estimation Methods*

Direct dynamical mass measurements of SMBHs require spatially resolved kinematics of stars or gas in the nuclear region, limiting such studies to nearby galaxies (Kormendy & Ho 2013). For AGN, the reverberation mapping technique provides the most reliable mass estimates by measuring the time delay τ between continuum and emission line variations, which directly probes the light-travel time across the BLR (Blandford & McKee 1982; Peterson 1993). The black hole mass then follows from the virial theorem:

$$M_{\mathrm{BH}} = f \frac{c\tau \, \Delta V^2}{G}, \tag{1}$$

where ΔV is a characteristic velocity (FWHM or line dispersion σ_{line}), G is the gravitational constant, c is the speed of light, and f is a dimensionless virial factor encoding the unknown BLR geometry and kinematics (Onken et al. 2004; Woo et al. 2010; Grier et al. 2013).

Reverberation mapping campaigns have established an empirical correlation between the BLR radius and AGN luminosity—the R–L relation (Kaspi et al. 2000, 2005; Bentz et al. 2013):

$$R_{\mathrm{BLR}} \propto L^{0.5}, \tag{2}$$

where L is typically the continuum luminosity at 5100 Å or the broad Hβ luminosity. This relation enables single-epoch (SE) virial mass estimates from a single spectrum, making black hole mass measurements feasible for large AGN samples (Vestergaard & Peterson 2006; Greene & Ho 2005; Shen et al. 2011).

1.4. *Objectives and Paper Structure*

In this paper, we present a detailed spectroscopic analysis of the Type-1 quasar SDSS J000111 at $z = 0.5178$. Our objectives are: (1) to perform comprehensive multi-component spectral fitting of both the Hβ and Hα spectral regions; (2) to measure the broad-line widths and derive black hole mass estimates using multiple calibrations; and (3) to assess the systematic uncertainties and consistency between different mass estimators.

This paper is organized as follows. Section 2 describes the observational data and target properties. Section 3 details our spectral decomposition methodology. Section 4 presents the emission line measurements and black hole mass estimates. Section 5 discusses the implications of our results, and Section 6 summarizes our conclusions.

2. DATA

2.1. *Target Selection and Properties*

The target analyzed in this work is a Type-1 quasar identified in the Sloan Digital Sky Survey (York et al. 2000) with coordinates (J2000) $\alpha = 0.29666°$, $\delta = -0.33654°$ (equivalently, RA = $00^{\mathrm{h}}01^{\mathrm{m}}11.20^{\mathrm{s}}$, Dec = $-00°20'11.5''$). The source was selected from the SDSS SkyServer database using the Visual Tools "Explore" interface, chosen for its clear emission line features and high signal-to-noise ratio spectrum suitable for detailed spectral decomposition.

The spectroscopic redshift of $z = 0.5178216$ was adopted from the SDSS pipeline, determined through cross-correlation with quasar templates (Bolton et al. 2012). At this redshift, both the Hβ–[O III] complex ($\lambda_{\mathrm{rest}} \sim 4700$–5100 Å) and the H$\alpha$–[N II]–[S II] complex ($\lambda_{\mathrm{rest}} \sim 6400$–6800 Å) fall within the BOSS wavelength coverage, enabling simultaneous analysis of both Balmer lines.

2.2. *SDSS/BOSS Observations*

The spectrum was obtained as part of the Baryon Oscillation Spectroscopic Survey (BOSS; Dawson et al. 2013), a component of SDSS-III that obtained optical spectroscopy for over 1.5 million galaxies and 160,000 quasars. BOSS observations were conducted using the upgraded SDSS spectrographs on the 2.5-meter Sloan Foundation Telescope at Apache Point Observatory in New Mexico (Gunn et al. 2006; Smee et al. 2013).

The telescope operates at a focal ratio of $f/5$ with a field of view of 3° diameter. The BOSS spectrographs provide wavelength coverage from 3600 to 10400 Å with a resolving power ranging from $R \sim 1560$ at the blue end to $R \sim 2650$ at the red end, corresponding to velocity resolutions of $\sim 190\ \mathrm{km\,s^{-1}}$ to $\sim 110\ \mathrm{km\,s^{-1}}$ (Smee et al. 2013). The focal plane utilizes aluminum plug plates pre-drilled with ~ 1000 holes at the precise coordinates of target objects. Optical fibers with diameters of 2$''$ (corresponding to ~ 13 kpc at $z = 0.52$) are plugged into these holes to collect light from individual targets (Dawson et al. 2013).

The observation metadata, including the Modified Julian Date (MJD), plate number, fiber identification, and exposure time, are summarized in Table 2.

2.3. *Data Reduction*

Spectroscopic data were retrieved from the SDSS Science Archive Server in pipeline-reduced, flux-calibrated

form. The SDSS spectroscopic pipeline (Bolton et al. 2012) performs standard reduction procedures including bias subtraction, flat-fielding, wavelength calibration using arc lamp exposures, optimal sky subtraction, and spectrophotometric flux calibration. The pipeline delivers extracted one-dimensional spectra with associated inverse-variance arrays encoding per-pixel uncertainties.

The SDSS provides wavelengths in logarithmic units (vacuum wavelengths). We converted to linear wavelength scale via

$$\lambda_{\mathrm{obs}} = 10^{\mathrm{loglam}}, \tag{3}$$

where "loglam" is the SDSS wavelength array. The rest-frame transformation was then applied using the catalog redshift:

$$\lambda_{\mathrm{rest}} = \frac{\lambda_{\mathrm{obs}}}{1+z}, \tag{4}$$

with $z = 0.5178216$. This correction shifts all spectral features to their intrinsic laboratory wavelengths and is essential for accurate emission line identification and measurement.

2.4. *Galactic Extinction Correction*

We corrected the observed spectrum for Milky Way foreground dust extinction using the Fitzpatrick (1999) extinction law with a total-to-selective extinction ratio of $R_V = 3.1$. Because extinction operates in the observer's frame, rest-frame wavelengths were first converted back to observed wavelengths for the extinction calculation.

The line-of-sight color excess $E(B-V)$ was obtained from the Schlegel et al. (1998) infrared dust emission maps using the `sfdmap` Python package:

$$E(B-V) = \mathrm{SFD}(\alpha, \delta), \tag{5}$$

where SFD denotes the Schlegel, Finkbeiner & Davis dust map value at the target coordinates. The V-band extinction follows as $A_V = R_V \times E(B-V) = 3.1 \times E(B-V)$.

The wavelength-dependent extinction $A(\lambda)$ was computed using the Fitzpatrick (1999) parameterization via the `extinction` Python library. The intrinsic (dereddened) flux density was recovered as

$$F_{\lambda,\mathrm{int}} = F_{\lambda,\mathrm{obs}} \times 10^{0.4 A(\lambda)}. \tag{6}$$

Uncertainties were propagated proportionally:

$$\sigma_{\mathrm{int}} = \sigma_{\mathrm{obs}} \times \frac{F_{\mathrm{int}}}{F_{\mathrm{obs}}}. \tag{7}$$

Pixels with zero flux were temporarily assigned small positive values to avoid numerical division errors during the dereddening calculation. After extinction correction, wavelengths were returned to the rest frame for all subsequent analysis.

3. METHODS

3.1. *Spectral Regions Analyzed*

We performed spectral decomposition in two wavelength regions:

1. **Hβ region** (rest-frame 4700–5100 Å): Contains the Hβ λ4861 emission line and the [O III] λλ4959,5007 forbidden doublet. This region provides the canonical broad Hβ line width measurement and the strong [O III] lines.

2. **Hα region** (rest-frame 6400–6800 Å): Contains the Hα λ6563 emission line, the [N II] λλ6548,6583 doublet, and the [S II] λλ6716,6731 doublet. This region provides an independent broad-line measurement and the narrow-line ratios.

The choice to analyze both Balmer lines serves multiple purposes. The Hβ line, together with the 5100 Å continuum luminosity, is the standard calibrator for reverberation-mapped mass relations (Kaspi et al. 2005; Bentz et al. 2013). The Hα line is intrinsically stronger (reducing measurement uncertainties), less affected by dust extinction, and provides a robust cross-check when Hβ is weak or blended with Fe II emission. Using both lines reduces systematic uncertainties in single-epoch mass estimates (Greene & Ho 2005).

3.2. *Continuum Modeling*

3.2.1. *Power-Law AGN Continuum*

The AGN optical–UV continuum is well-described by a power law arising from thermal emission across the accretion disk (Shakura & Sunyaev 1973). The multi-temperature blackbody emission from annuli at different disk radii superimposes to produce a characteristic power-law spectrum:

$$F_\nu \propto \nu^\alpha, \tag{8}$$

where the spectral index α reflects the temperature profile and radiative efficiency of the disk. Even sophisticated disk atmosphere models retain this approximate power-law form over broad wavelength ranges (Davis & Laor 2011).

Additionally, AGN exhibit non-thermal emission from Comptonization in the hot corona, which also produces power-law spectra due to the underlying power-law distribution of electron energies (Haardt & Maraschi 1991). Empirically, decades of AGN spectroscopy have confirmed that the optical–UV continuum is well-approximated by a power law (Vanden Berk et al. 2001), making this model physically justified and statistically robust.

We modeled the continuum in each spectral region as

$$F_\lambda^{\mathrm{PL}} = A \left(\frac{\lambda}{\lambda_0} \right)^{-\alpha}, \qquad (9)$$

where A is the normalization amplitude at reference wavelength λ_0 and α is the spectral index. Both parameters were treated as free in the fit.

3.2.2. *Stellar Template*

Host galaxy starlight contributes continuum emission and absorption features that must be removed to isolate the AGN components. We employed stellar population templates from the MILES (Medium-resolution Isaac Newton Telescope Library of Empirical Spectra) library (Sánchez-Blázquez et al. 2006; Falcón-Barroso et al. 2011). The MILES templates provide high-quality empirical spectra covering a range of stellar ages and metallicities at spectral resolution comparable to SDSS.

The stellar template contribution was modeled as

$$F_\lambda^\star = s_\star \, T_\star(\lambda - \Delta\lambda_\star), \qquad (10)$$

where $s_\star$ is the scaling amplitude, $T_\star(\lambda)$ is the template spectrum interpolated to the appropriate stellar age, and $\Delta\lambda_\star$ allows for a small velocity shift. The template age was treated as a free parameter to account for variations in host galaxy stellar populations.

3.2.3. *Fe II Pseudo-Continuum Template*

The Fe II emission complex arises from thousands of blended transitions in the BLR, producing a characteristic pseudo-continuum that overlaps significantly with the Hβ and Hα regions (Boroson & Green 1992; Vestergaard & Wilkes 2001). Failure to account for Fe II emission biases the measurement of Balmer line widths and fluxes required for mass estimation.

We employed an empirical Fe II template with free scaling, velocity broadening, and wavelength shift parameters:

$$F_\lambda^{\mathrm{Fe\ II}} = s_{\mathrm{Fe}} \, T_{\mathrm{Fe}}(\lambda - \Delta\lambda_{\mathrm{Fe}}), \qquad (11)$$

where the template $T_{\mathrm{Fe}}(\lambda)$ was convolved to match the instrumental resolution. Including the Fe II template ensures that the remaining emission-line profiles represent the intrinsic Balmer emission suitable for reliable fitting (Boroson & Green 1992; Sánchez-Blázquez et al. 2006).

3.3. *Emission Line Modeling*

3.3.1. *Gaussian Line Profiles*

Emission lines were modeled using Gaussian functions, which provide physically motivated and empirically successful descriptions of the velocity distributions in AGN emission regions. Gas in both the BLR and NLR exhibits random, virial, or turbulent motions that produce approximately Gaussian line shapes (Peterson et al. 2004; Greene & Ho 2005):

$$G(\lambda) = B \exp\left[-\frac{(\lambda - \lambda_0)^2}{2\sigma^2} \right], \qquad (12)$$

where B is the peak amplitude, λ_0 is the central wavelength, and the standard deviation σ relates to the FWHM by

$$\mathrm{FWHM} = 2\sqrt{2\ln 2}\,\sigma \approx 2.355\sigma. \qquad (13)$$

3.3.2. *Narrow Emission Lines*

Each narrow emission line was fitted with two Gaussian components representing a "core plus wing" structure. This decomposition is necessary because real narrow lines often exhibit asymmetric profiles with extended wings associated with NLR outflows or stratified kinematics (Mullaney et al. 2013). A single Gaussian cannot simultaneously reproduce both the sharp core and extended wings, whereas a two-Gaussian model captures the full profile without overfitting and is standard in the literature (Vestergaard & Peterson 2006).

For the [O III] $\lambda\lambda4959,5007$ doublet, we fixed the flux ratio at the theoretical value $f_{5007}/f_{4959} = 2.98$ based on atomic physics (Storey & Zeippen 2000). The velocity widths and offsets of corresponding components were tied between the two lines. Similar constraints were applied to the [N II] $\lambda\lambda6548,6583$ doublet (theoretical ratio $f_{6583}/f_{6548} = 2.96$) and the [S II] $\lambda\lambda6716,6731$ doublet.

The narrow Hβ and Hα components were tied in velocity width and offset to the narrow [O III] and [N II] components, respectively, ensuring consistent NLR kinematics across all narrow lines.

3.3.3. *Broad Emission Lines*

The broad Hβ and Hα emission lines were each modeled with a single Gaussian component. The BLR produces very wide (~ 1000–10000 km s^{-1}), smooth, and relatively symmetric profiles dominated by high-velocity, gravitationally bound gas. At SDSS resolution, a single Gaussian adequately describes the broad Balmer line shapes for the purposes of measuring width and flux, while additional components would introduce degeneracy without meaningful improvement in fit quality. This approach provides a clean, physically interpretable decomposition of both narrow and broad emission-line regions.

The broad-line parameters (amplitude, central wavelength, FWHM) were left unconstrained to capture the full range of BLR kinematics.

3.4. *Full Spectral Model*

The complete model for each spectral region is the sum of all components:

$$F_{\mathrm{model}}(\lambda) = F_{\mathrm{PL}}(\lambda) + F_{\star}(\lambda) + F_{\mathrm{Fe\,II}}(\lambda)$$
$$+ \sum_j G_j^{\mathrm{narrow}}(\lambda) + G^{\mathrm{broad}}(\lambda) \quad (14)$$

where the sum runs over all narrow-line Gaussian components.

For the Hβ region, the model includes:

- Power-law continuum (2 parameters: amplitude, slope)

- Stellar template (3 parameters: scale, age index, velocity shift)

- Fe II template (3 parameters: scale, broadening, shift)

- Broad Hβ (3 parameters: amplitude, centroid, FWHM)

- Narrow Hβ (2 components × 3 parameters, with ties)

O III λ4959 (2 components, tied to λ5007)

O III λ5007 (2 components × 3 parameters)

For the Hα region, the model includes analogous components for the power-law, templates, broad Hα, narrow Hα, [N II] doublet, and [S II] doublet.

3.5. *Fitting Procedure*

Spectral fitting was performed using custom AGN spectral decomposition routines built on the `pyspeckit` package (Ginsburg & Mirocha 2011) with a Levenberg–Marquardt nonlinear least-squares optimizer (Markwardt 2009). The objective function minimized was the χ^2 statistic:

$$\chi^2 = \sum_i \frac{[F_{\mathrm{obs}}(\lambda_i) - F_{\mathrm{model}}(\lambda_i)]^2}{\sigma_i^2}, \quad (15)$$

where σ_i are the per-pixel uncertainties from the SDSS inverse-variance array.

The fitting was performed iteratively, with the number of iterations chosen to ensure convergence while avoiding overfitting. For the Hβ region, 35 iterations were required to achieve stable parameter values. The Hα region, with its stronger lines and simpler blending structure, converged in only 2 iterations.

Parameter uncertainties were estimated from the covariance matrix returned by the optimizer, scaled by the reduced χ^2 to account for potential error underestimation:

$$\sigma_p = \sqrt{C_{pp} \cdot \chi_\nu^2}, \quad (16)$$

where C_{pp} is the diagonal covariance element for parameter p and $\chi_\nu^2 = \chi^2/(N_{\mathrm{data}} - N_{\mathrm{param}})$.

4. RESULTS

4.1. *Continuum and Template Fit Results*

Table 3 presents the best-fit continuum and template parameters for both spectral regions.

In the Hβ region, the power-law continuum has amplitude $A = 62.21 \times 10^{-17}$ erg s^{-1} cm^{-2} Å^{-1} and spectral index $\alpha = -1.03$. The negative spectral index indicates a red continuum slope, which may reflect host galaxy contamination or dust reddening beyond the Galactic foreground correction.

In the Hα region, the power-law parameters are $A = 1.43 \times 10^{-17}$ erg s^{-1} cm^{-2} Å^{-1} and $\alpha = -1.50$. The steeper red slope at longer wavelengths is consistent with expectations for composite AGN+host spectra.

The stellar template contributes significantly in both regions, with ages of $\sim$ 11–13 Gyr indicating an old stellar population in the host galaxy. The Fe II template contribution is modest, consistent with the relatively narrow Fe II features in this source.

4.2. *Emission Line Measurements*

Table 4 presents the complete emission line parameters from the spectral decomposition.

4.2.1. *Hβ Region*

The broad Hβ component is well-detected with central wavelength $\lambda_0 = 4868.1$ Å, FWHM = 4277.3 km s^{-1}, and integrated flux $F_{\mathrm{H\beta,b}} = 7.2 \times 10^{-17}$ erg s^{-1} cm^{-2}. The broad component dominates the Hβ profile, as expected for a Type-1 quasar.

The [O III] λ5007 line shows a strong core component with FWHM = 352.5 km s^{-1} and flux 33.6 × 10^{-17} erg s^{-1} cm^{-2}, plus a broader wing component with FWHM = 660.4 km s^{-1} and flux 4.0 × 10^{-17} erg s^{-1} cm^{-2}. The presence of the wing component indicates NLR outflows or complex kinematics.

4.2.2. *Hα Region*

The broad Hα component has central wavelength $\lambda_0 = 6550.8$ Å, FWHM = 4706.5 km s^{-1}, and integrated flux $F_{\mathrm{H\alpha,b}} = 28.7 \times 10^{-17}$ erg s^{-1} cm^{-2}. The broad Hα/Hβ flux ratio of $\sim$ 4 is consistent with Case B recombination with modest dust extinction.

The FWHM values of the broad Hα and Hβ lines are consistent within $\sim$ 10% (4707 vs. 4277 km s^{-1}), supporting the assumption that both lines originate from the same BLR gas.

The narrow Hα component has FWHM $= 388.4$ km s^{-1} and flux 23.5×10^{-17} erg s^{-1} cm^{-2}. The [N II] $\lambda6583$ line has flux 31.6×10^{-17} erg s^{-1} cm^{-2}, and [S II] $\lambda6716$ has flux 11.8×10^{-17} erg s^{-1} cm^{-2}.

Figure 1 shows the observed spectrum and best-fit model for the Hβ region, with individual components displayed. Figure 2 shows the corresponding fit for the Hα region.

4.3. *Black Hole Mass Estimation*

We derived single-epoch black hole masses using multiple calibrations from the literature to assess systematic uncertainties.

4.3.1. *Hα-Based Mass Estimate*

Following Greene & Ho (2005), the black hole mass from the broad Hα line is

$$M_{\rm BH} = (2.0^{+0.4}_{-0.3}) \times 10^6 \left(\frac{L_{\rm H\alpha}}{10^{42} \text{ erg s}^{-1}} \right)^{0.55 \pm 0.02} \\ \times \left(\frac{\text{FWHM}_{\rm H\alpha}}{10^3 \text{ km s}^{-1}} \right)^{2.06 \pm 0.06} M_\odot \tag{17}$$

The Hα luminosity was computed from the integrated broad-line flux:

$$L_{\rm H\alpha} = 4\pi D_L^2 F_{\rm H\alpha,b}, \tag{18}$$

where D_L is the luminosity distance at $z = 0.5178$. Adopting a flat ΛCDM cosmology with $H_0 = 70$ km s^{-1} Mpc^{-1} and $\Omega_m = 0.3$, we obtain $D_L = 2.98$ Gpc.

Using our measured values of $\text{FWHM}_{\rm H\alpha} = 4706.5$ km s^{-1} and $F_{\rm H\alpha,b} = 28.7 \times 10^{-17}$ erg s^{-1} cm^{-2}, we derive

$$M_{\rm BH}(\text{H}\alpha) = 2.39 \times 10^6 \ M_\odot. \tag{19}$$

4.3.2. *Hβ-Based Mass Estimates*

The Hβ line luminosity-based calibration from Greene & Ho (2005) is

$$M_{\rm BH} = (3.6 \pm 0.2) \times 10^6 \left(\frac{L_{\rm H\beta}}{10^{42} \text{ erg s}^{-1}} \right)^{0.56 \pm 0.02} \\ \times \left(\frac{\text{FWHM}_{\rm H\beta}}{10^3 \text{ km s}^{-1}} \right)^2 M_\odot \tag{20}$$

Using $\text{FWHM}_{\rm H\beta} = 4277.3$ km s^{-1} and $F_{\rm H\beta,b} = 7.2 \times 10^{-17}$ erg s^{-1} cm^{-2}, we obtain

$$M_{\rm BH}(\text{H}\beta, L_{\rm H\beta}) = 1.49 \times 10^7 \ M_\odot. \tag{21}$$

We also computed masses using the 5100 Å continuum luminosity-based calibrations. Following Vestergaard & Peterson (2006), the "local" calibration gives

$$M_{\rm BH}^{\rm local} = 5.26 \times 10^6 \left(\frac{L_{5100}}{10^{44} \text{ erg s}^{-1}} \right)^{0.65} \\ \times \left(\frac{\text{FWHM}_{\rm H\beta}}{10^3 \text{ km s}^{-1}} \right)^2 M_\odot \tag{22}$$

yielding $M_{\rm BH}^{\rm local} = 8.96 \times 10^8 \ M_\odot$.

The "global" calibration gives

$$M_{\rm BH}^{\rm global} = 7.17 \times 10^6 \left(\frac{L_{5100}}{10^{44} \text{ erg s}^{-1}} \right)^{0.58} \\ \times \left(\frac{\text{FWHM}_{\rm H\beta}}{10^3 \text{ km s}^{-1}} \right)^2 M_\odot \tag{23}$$

yielding $M_{\rm BH}^{\rm global} = 9.61 \times 10^8 \ M_\odot$.

4.3.3. *Summary of Mass Estimates*

Table 1 summarizes the black hole mass estimates from different calibrations:

Table 1. Black Hole Mass Estimates

Calibration	$M_{\rm BH}$ ($M_\odot$)
Hα (Greene & Ho 2005)	2.39×10^6
Hβ, $L_{\rm H\beta}$ (Greene & Ho 2005)	1.49×10^7
Hβ, L_{5100} local (Vestergaard & Peterson 2006)	8.96×10^8
Hβ, L_{5100} global (Vestergaard & Peterson 2006)	9.61×10^8

The mass estimates span nearly three orders of magnitude, from $\sim 10^{6.4}$ to $\sim 10^{9.0} \ M_\odot$. This large range reflects the well-known systematic uncertainties in single-epoch mass calibrations, which we discuss further in Section 5.

5. DISCUSSION

5.1. *Discrepancies Between Mass Estimators*

The black hole mass estimates derived from different calibrations span nearly three orders of magnitude, from $M_{\rm BH} \sim 2 \times 10^6 \ M_\odot$ (Hα-based) to $M_{\rm BH} \sim 10^9 \ M_\odot$ (continuum luminosity-based). This large discrepancy warrants careful examination.

The Hα-based estimate is systematically lower than the Hβ-based estimates by a factor of ~ 6. This difference may arise from several effects: (1) differential dust extinction between the two lines, though Hα should be *less* affected; (2) differences in the BLR stratification probed by each line; (3) systematic offsets in the calibration samples used to derive the scaling relations; or (4) the presence of a narrow Hα component that was not fully separated from the broad component.

The dramatically larger masses from the continuum luminosity-based calibrations ($\sim 10^9\ M_\odot$) compared to the line luminosity-based estimates ($\sim 10^{6-7}\ M_\odot$) likely reflect host galaxy contamination of the 5100 Å continuum. At $z = 0.52$, the $2''$ BOSS fiber encompasses ~ 13 kpc, including substantial host galaxy light that inflates the apparent AGN continuum luminosity. The negative power-law slopes ($\alpha < 0$) found in our continuum fits support this interpretation, as pure AGN continua typically have $\alpha > 0$ (blue slopes).

The line luminosity-based masses are likely more reliable for this source, as they are less susceptible to host contamination. We adopt the Hβ line luminosity-based value of $M_{\rm BH} \sim 1.5 \times 10^7\ M_\odot$ as our best estimate, with systematic uncertainties of at least ~ 0.5 dex.

5.2. *Quality of the Spectral Decomposition*

The spectral fits achieved good residuals in both the Hβ and Hα regions, validating the adopted model complexity. The use of two Gaussian components for each narrow line successfully captured the core-plus-wing structure evident in the [O III] and [N II] profiles. The single Gaussian model for the broad lines provided adequate fits given the SDSS spectral resolution.

The narrow-line components show somewhat different properties between the Hβ and Hα regions. The [O III] lines are notably stronger relative to H$\beta_{\rm narrow}$ than the [N II] lines relative to H$\alpha_{\rm narrow}$. This is physically expected given the high ionization potential required to produce [O III] in AGN-ionized gas.

The Fe II contribution was modest in this source, simplifying the decomposition in the Hβ region. Sources with stronger Fe II emission require more careful treatment to avoid biasing the broad Hβ measurement.

5.3. *Future Prospects*

Several avenues could improve the black hole mass estimate for this source:

1. **Host galaxy decomposition**: Spatially resolved imaging or spectral decomposition to separate host and AGN continuum contributions would enable more reliable continuum luminosity-based mass estimates.

2. **Markov chain Monte Carlo**: Performing MCMC can be done next to lower the uncertainty. For now we are using the values without uncertainties directly to estimate the mass.

3. **Multi-epoch monitoring**: Reverberation mapping would provide a direct BLR radius measure-

ment, eliminating the dominant uncertainty in single-epoch estimates.

4. **High-resolution spectroscopy**: Better spectral resolution would enable more detailed decomposition of the broad-line profiles, potentially revealing multiple kinematic components.

5. **Coronal line analysis**: Detection of coronal emission lines (e.g., [Fe VII], [Fe X]) in deep spectroscopy could probe the innermost regions of the AGN and provide independent constraints on the ionizing continuum shape.

6. SUMMARY AND CONCLUSIONS

We have presented a comprehensive spectroscopic analysis of the Type-1 quasar SDSS J000111 at $z = 0.5178$. Our main findings are:

1. Multi-component spectral decomposition of both the Hβ–[O III] and Hα–[N II]–[S II] regions successfully isolated broad and narrow emission line components, along with power-law continuum, stellar, and Fe II template contributions.

2. The broad Hβ line has FWHM = 4277 km s^{-1}, and the broad Hα line has FWHM = 4707 km s^{-1}. The consistency between these measurements supports the assumption that both lines originate from the same virialized BLR gas.

3. Black hole mass estimates range from $M_{\rm BH} \sim 2 \times 10^6\ M_\odot$ (Hα-based) to $\sim 10^9\ M_\odot$ (continuum-based), reflecting large systematic uncertainties. We adopt $M_{\rm BH} \sim 1.5 \times 10^7\ M_\odot$ from the Hβ line luminosity calibration as our best estimate.

4. The large discrepancy between continuum-based and line-based mass estimates likely reflects host galaxy contamination of the 5100 Å continuum in this moderate-redshift source.

This analysis demonstrates the importance of using multiple mass calibrations and emission lines to assess systematic uncertainties in single-epoch black hole mass estimates.

REFERENCES

Antonucci, R. 1993, ARA&A, 31, 473,
doi: 10.1146/annurev.aa.31.090193.002353

Antonucci, R. R. J., & Miller, J. S. 1985, ApJ, 297, 621,
doi: 10.1086/163559

Astropy Collaboration, Price-Whelan, A. M., Sipőcz, B. M.,
et al. 2018, AJ, 156, 123, doi: 10.3847/1538-3881/aabc4f

Astropy Collaboration, Robitaille, T. P., Tollerud, E. J.,
et al. 2013, A&A, 558, A33,
doi: 10.1051/0004-6361/201322068

Bentz, M. C., Denney, K. D., Grier, C. J., et al. 2013, ApJ,
767, 149, doi: 10.1088/0004-637X/767/2/149

Blandford, R. D., & McKee, C. F. 1982, ApJ, 255, 419,
doi: 10.1086/159843

Bolton, A. S., Schlegel, D. J., Aubourg, É., et al. 2012, AJ,
144, 144, doi: 10.1088/0004-6256/144/5/144

Boroson, T. A., & Green, R. F. 1992, ApJS, 80, 109,
doi: 10.1086/191661

Davis, S. W., & Laor, A. 2011, ApJ, 728, 98,
doi: 10.1088/0004-637X/728/2/98

Dawson, K. S., Schlegel, D. J., Ahn, C. P., et al. 2013, AJ,
145, 10, doi: 10.1088/0004-6256/145/1/10

Falcón-Barroso, J., Sánchez-Blázquez, P., Vazdekis, A.,
et al. 2011, A&A, 532, A95,
doi: 10.1051/0004-6361/201116842

Fitzpatrick, E. L. 1999, PASP, 111, 63, doi: 10.1086/316293

Ginsburg, A., & Mirocha, J. 2011, Astrophysics Source
Code Library, ascl:1109.001

Greene, J. E., & Ho, L. C. 2005, ApJ, 630, 122,
doi: 10.1086/431897

Grier, C. J., Peterson, B. M., Horne, K., et al. 2013, ApJ,
764, 47, doi: 10.1088/0004-637X/764/1/47

Gunn, J. E., Siegmund, W. A., Mannery, E. J., et al. 2006,
AJ, 131, 2332, doi: 10.1086/500975

Haardt, F., & Maraschi, L. 1991, ApJL, 380, L51,
doi: 10.1086/186171

Harris, C. R., Millman, K. J., van der Walt, S. J., et al.
2020, Nature, 585, 357, doi: 10.1038/s41586-020-2649-2

Hunter, J. D. 2007, Computing in Science and Engineering,
9, 90, doi: 10.1109/MCSE.2007.55

Kaspi, S., Maoz, D., Netzer, H., et al. 2005, ApJ, 629, 61,
doi: 10.1086/431275

Kaspi, S., Smith, P. S., Netzer, H., et al. 2000, ApJ, 533,
631, doi: 10.1086/308704

Kormendy, J., & Ho, L. C. 2013, ARA&A, 51, 511,
doi: 10.1146/annurev-astro-082708-101811

Markwardt, C. B. 2009, Astronomical Data Analysis
Software and Systems XVIII, 411, 251

Mullaney, J. R., Alexander, D. M., Fine, S., et al. 2013,
MNRAS, 433, 622, doi: 10.1093/mnras/stt751

Netzer, H. 2015, ARA&A, 53, 365,
doi: 10.1146/annurev-astro-082214-122302

Onken, C. A., Ferrarese, L., Merritt, D., et al. 2004, ApJ,
615, 645, doi: 10.1086/424655

Peterson, B. M. 1993, PASP, 105, 247, doi: 10.1086/133140

Peterson, B. M., Ferrarese, L., Gilbert, K. M., et al. 2004,
ApJ, 613, 682, doi: 10.1086/423269

Sánchez-Blázquez, P., Peletier, R. F., Jiménez-Vicente, J.,
et al. 2006, MNRAS, 371, 703,
doi: 10.1111/j.1365-2966.2006.10699.x

Schlegel, D. J., Finkbeiner, D. P., & Davis, M. 1998, ApJ,
500, 525, doi: 10.1086/305772

Schmidt, M. 1963, Nature, 197, 1040,
doi: 10.1038/1971040a0

Shakura, N. I., & Sunyaev, R. A. 1973, A&A, 24, 337

Shen, Y., Richards, G. T., Strauss, M. A., et al. 2011,
ApJS, 194, 45, doi: 10.1088/0067-0049/194/2/45

Smee, S. A., Gunn, J. E., Uomoto, A., et al. 2013, AJ, 146,
32, doi: 10.1088/0004-6256/146/2/32

Storey, P. J., & Zeippen, C. J. 2000, MNRAS, 312, 813,
doi: 10.1046/j.1365-8711.2000.03184.x

Urry, C. M., & Padovani, P. 1995, PASP, 107, 803,
doi: 10.1086/133630

Vanden Berk, D. E., Richards, G. T., Bauer, A., et al. 2001,
AJ, 122, 549, doi: 10.1086/321167

Vestergaard, M., & Peterson, B. M. 2006, ApJ, 641, 689,
doi: 10.1086/500572

Vestergaard, M., & Wilkes, B. J. 2001, ApJS, 134, 1,
doi: 10.1086/320357

Virtanen, P., Gommers, R., Oliphant, T. E., et al. 2020,
Nature Methods, 17, 261, doi: 10.1038/s41592-019-0686-2

Woo, J.-H., Treu, T., Barth, A. J., et al. 2010, ApJ, 716,
269, doi: 10.1088/0004-637X/716/1/269

York, D. G., Adelman, J., Anderson, Jr., J. E., et al. 2000,
AJ, 120, 1579, doi: 10.1086/301513

Table 2. Observation Log for SDSS J000111

Parameter	Value
R.A. (J2000)	$0.29666°$
Dec. (J2000)	$-0.33654°$
Redshift (z)	0.5178216
Plate	4216
MJD	55477
Fiber ID	0224
Survey	BOSS

Table 3. Continuum and Template Parameters from Spectral Decomposition

| Region	Parameter	Value	Units
Power-Law Continuum			
Hβ	Scale (A)	62.21	10^{-17} erg s^{-1} cm^{-2} Å^{-1}
Hβ	Index (α)	-1.03	—
Hα	Scale (A)	1.43	10^{-17} erg s^{-1} cm^{-2} Å^{-1}
Hα	Index (α)	-1.50	—
Stellar Template (MILES)			
Hβ	Scale	1.32	10^{-17} erg s^{-1} cm^{-2} Å^{-1}
Hβ	Age	12.5	Gyr
Hα	Scale	14.60	10^{-17} erg s^{-1} cm^{-2} Å^{-1}
Hα	Age	11.62	Gyr

Table 4. Emission Line Parameters from Spectral Decomposition

Component	Central λ (Å)	FWHM (km s^{-1})	Integrated Flux (10^{-17} erg s^{-1} cm^{-2})
Hβ Region			
Hβ narrow 1	4994.9	503.5 (fixed)	0.98
Hβ narrow 2	5006.6	503.5 (fixed)	32.78
Hβ broad	4868.1	4277.3	7.2
[O III] λ4959 n1	4959.2 (fixed)	352.5 (fixed)	11.2
[O III] λ4959 n2	4959.2 (fixed)	660.4 (fixed)	13.30
[O III] λ5007 n1	5006.5	660.4	4.0
[O III] λ5007 n2	5007.1	352.5	33.6
Hα Region			
[N II] λ6548	6548.3 (fixed)	388.4 (fixed)	10.8
[N II] λ6583	6582.9 (fixed)	388.4 (fixed)	31.6
Hα narrow	6562.2 (fixed)	388.4 (fixed)	23.5
Hα broad	6550.8	4706.5	28.7
[S II] λ6716	6716.1 (fixed)	388.4	11.8

Note—Parameters marked "(fixed)" were held constant during fitting. All the other parameters were also considered without uncertainties. Wavelengths are vacuum rest-frame values. "n1", "n2" denote narrow components; "broad" denotes the BLR component.
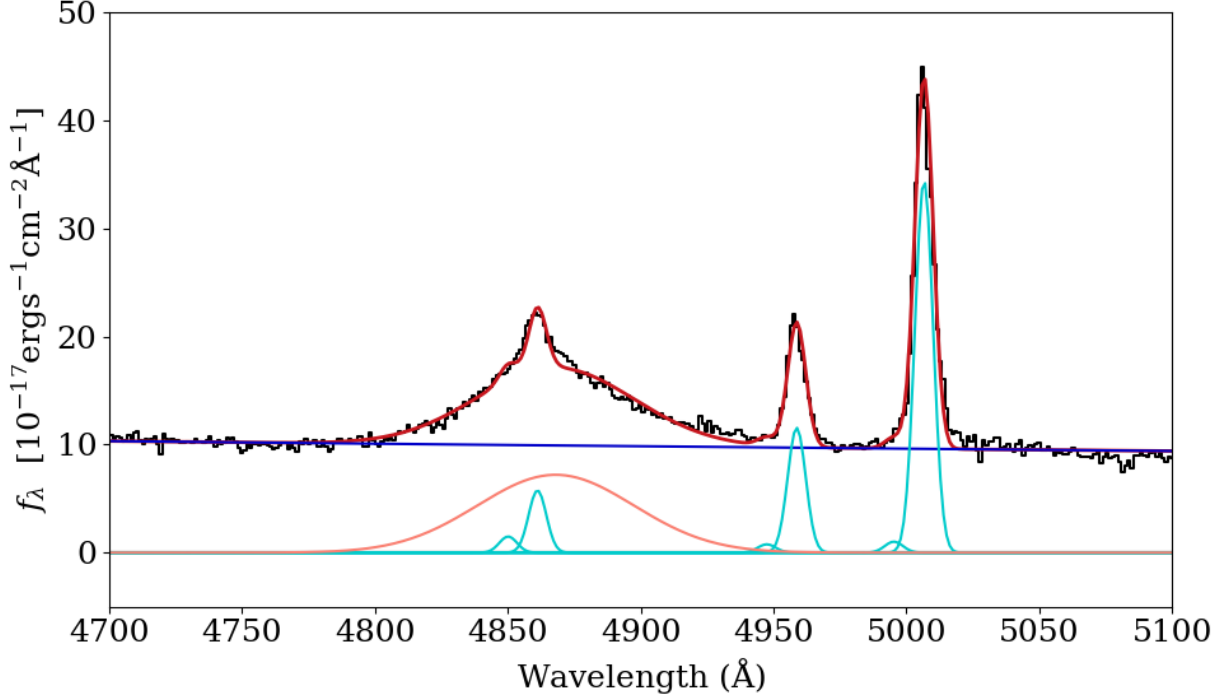
Figure 1. Spectral decomposition of the Hβ–[O III] region. *Top panel*: Observed spectrum (black histogram) with error envelope (gray shading) and best-fit total model (red). Individual components shown include the power-law continuum (orange), stellar template (brown), broad Hβ (cyan), narrow [O III] components (blue), and Fe II template. *Bottom panel*: Best-fit model with emission line components highlighted. The broad Hβ component dominates near 4861 Å, while the strong [O III] doublet peaks near 4959 and 5007 Å.
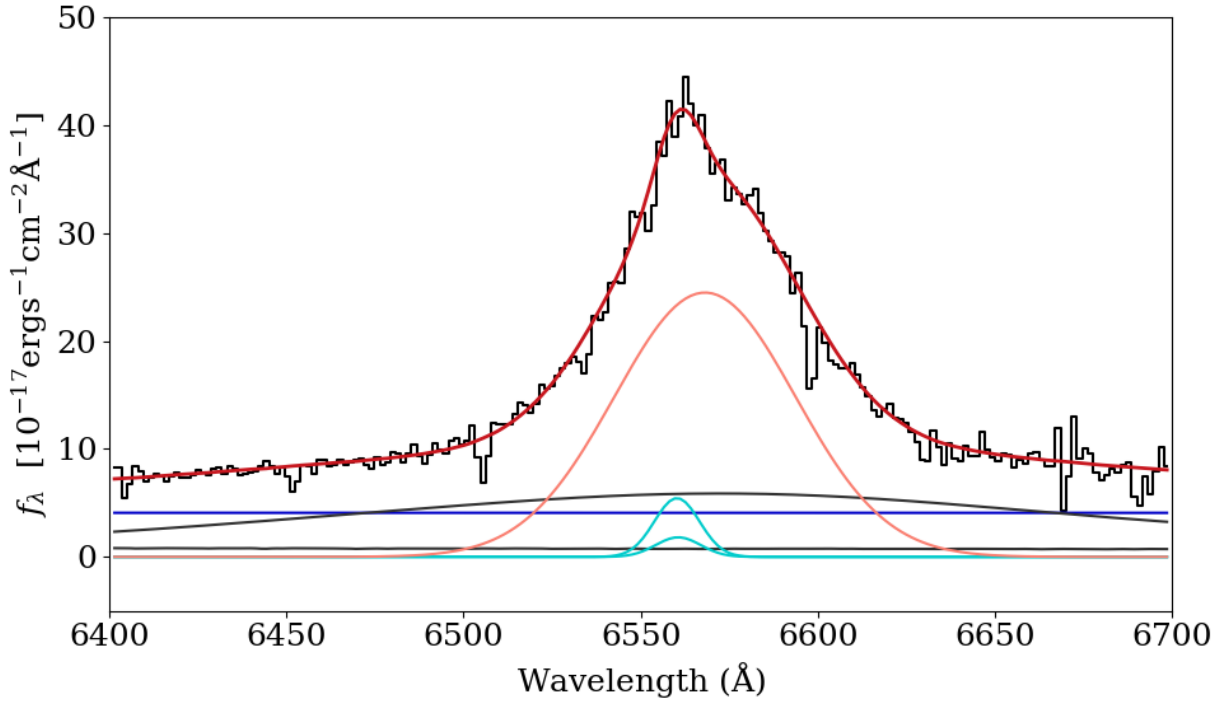
Figure 2. Spectral decomposition of the Hα–[N II]–[S II] region. Format as in Figure 1. The broad Hα component is blended with the narrow Hα and [N II] doublet. The [S II] doublet is visible at the red end of the fitting window.